

# Analysis of volumetric 3D reconstruction of lamina cribrosa images from swept-source optical coherence tomography in glaucomatous and healthy subjects

JUTAMASH WONGWAI,<sup>1</sup> PRATHAN BURANASIRI,<sup>1,2</sup>  KITSUCHART PASUPA,<sup>3,\*</sup>  AND ANITA MANASSAKORN<sup>4</sup>

<sup>1</sup>Artificial Intelligence Photonics Advanced Research Laboratory, Department of Physics, School of Science, King Mongkut's Institute of Technology Ladkrabang, Bangkok 10520, Thailand

<sup>2</sup>Electronic and Optoelectronic Device Research Unit, School of Science, King Mongkut's Institute of Technology Ladkrabang, Bangkok 10520, Thailand

<sup>3</sup>School of Information Technology, King Mongkut's Institute of Technology Ladkrabang, Bangkok 10520, Thailand

<sup>4</sup>Center of Excellence in Glaucoma, Department of Ophthalmology, Faculty of Medicine, Chulalongkorn University and King Chulalongkorn Memorial Hospital, The Thai Red Cross Society, Bangkok 10330, Thailand

\*[kitsuchart@it.kmitl.ac.th](mailto:kitsuchart@it.kmitl.ac.th)

**Abstract:** This study demonstrates the 3D visualization of the lamina cribrosa (LC) structure and its correlation with volumetric data, pore volume, and disc area in glaucomatous and non-glaucomatous eyes. The participant cohort included 65 glaucomatous and 58 non-glaucomatous eyes (13 suspected glaucoma and 45 normal). An ophthalmologist diagnosed glaucoma patients and all subjects were over 18 years old, passed a visual field test, and underwent optical coherence tomography (OCT) examinations. LC images were obtained using the DRI OCT Triton, while optic disc images were obtained from the enface image of the Cirrus HD-OCT 5000. Since LC images alone did not provide clear edge information, we used optic disc images as a reference for edge detection. To achieve this, we employed a fine-tuned model, specifically a pre-trained U-shaped Encoder-Decoder Network with Attention. This model was used to obtain a segmented mask, which was then aligned and utilized to locate the edge of the LC in the LC images. A blood vessel mask was created to remove blood vessels, as they can interfere with the accurate visualization and analysis of LC characteristics. This step allowed for the 3D reconstruction of the LC structure without the presence of blood vessels. Correlations between LC volume, pore volume, and pore volume to LC volume were calculated separately for glaucomatous and non-glaucomatous eyes. We divided the areas for considering the LC structure into three types: overall, quadrants, and 12-clock-hour sectors. Based on the experimental results, we found that the pore volume and pore-to-LC volume were different between glaucoma and normal across all areas considered. In conclusion, this research generated 3D images of the LC from OCT images using computer techniques, showcasing a microstructure that closely resembles the actual LC. Statistical methods were employed to calculate and analyze the differences observed between the two groups of samples.

© 2023 Optica Publishing Group under the terms of the [Optica Open Access Publishing Agreement](#)

## 1. Introduction

Glaucoma is a disease that damages the optic nerve and leads to vision loss and blindness. Currently, it is one of the leading causes of irreversible blindness in the world [1–3]. In 2006, 60.5 million people were diagnosed with glaucoma, which is expected to increase to 79.6 million in 2020. Almost half of them are located in Asia. Approximately 11 million people around the

world are blind in both eyes. As glaucoma is asymptomatic, especially in the early stage, over 50% of patients with glaucoma remain undiagnosed as they do not seek ophthalmic examination. As a result, they are prone to lose sight before receiving proper treatment [4], highlighting the importance of early detection and management of glaucoma. In the diagnosis process for glaucoma, the ophthalmologist will typically measure intraocular pressure and examine the optic nerve head (ONH) and visual field through various investigation tools.

In glaucoma, the optic nerve tissue surrounding the ONH begins to deteriorate in accordance with the severity of the disease. Elevated intraocular pressure is a known risk factor for ONH deterioration. It compresses the lamina cribrosa (LC), a multi-layered mesh-like tissue located deep within the ONH. There are pores or narrow channels for the optic nerve and blood vessels to pass through. To detect degeneration of ONH, optical coherence tomography (OCT) is used. It is designed to take pictures deep under the surface level. The thickness of ONH and LC can then be examined. OCT can also help diagnose other eye diseases, such as clogged blood vessels in the retina, macular disease, retinal fibrosis, retinal detachment, and retinal blood vessel abnormalities.

Unfortunately, the image quality from currently available commercial OCT devices to visualize LC for glaucoma diagnosis, swept-source OCT (SS-OCT), is poor. When capturing images of the LC, the fine details and microstructures, such as the internal edges, anterior and posterior borders, and pores, are not clearly visible. As a result, it is necessary to improve the image quality of OCT devices to enhance the visibility of LC to improve the diagnosis. It may help to explain the pathogenesis of glaucoma. This can be done in two ways: (i) by improving the OCT engine to get better images or (ii) by improving the images.

OCT tools can be improved by applying an adaptive optics (AO) principle in the tools. The improvements by this method are high cost due to the need to add various devices to the system. At present, it is not used in the examination room. Only one company exports AO-OCT for research [5]. Thus, to reduce the cost of improving image quality in this study, we used computer techniques — image processing and machine learning. While image processing techniques are suitable for simple images [6], machine learning techniques can improve the accuracy and speed of image processing for very complex images. For example, when segmentation details in the image or the edge of the Region of Interest (ROI) are unclear, machine learning can help. Neural network models such as Artificial Neural Networks (ANN), Convolutional Neural Networks (CNN), and Recurrent Neural Networks (RNN) can be trained to improve the efficiency of image processing and enhance the accuracy of glaucoma diagnosis [7,8].

The main objective of this research is to achieve the three-dimensional visualization of the LC structure and obtain discriminant characteristics of the three-dimensional LC structure between glaucomatous and non-glaucomatous cases. The three-dimensional LC was reconstructed using images obtained from a commercial SS-OCT device. The study focused on extracting the following characteristics: (i) the volumetric data of the LC and the porosity within the LC for both glaucoma and healthy subjects, and (ii) investigating the relationship between the volumetric data of the LC structure and the porosity.

The rest of this paper is organized into the following sections: Related works in Section 2, reviewing relevant research and summarizing the advantages and limitations of those works; Section 3, Materials and methods, discussing the research process, consisting of data collection of samples from tools and techniques used; Section 4, reports the results and discussion, consisting of the clinical study results and the 3D structure of the sample; and Section 5, is the conclusion.

## 2. Related works

Tezel et al. [9] studied pore expansion within the LC in glaucoma patients, and Akagi et al. [10] studied pore changes within the LC in glaucoma patients and normal eye subjects. Tezel's team compared optic disc images of glaucoma patients over three years in the NIH Image program.

They found that the patterns of porosity within the LC changed among three patterns: circles, ovals, and stripes. The total pore area of the LC in patients increased. Akagi's team studied pore deformation within the LC using disc photography, scanning laser ophthalmoscopy (SLO), and adaptive optics scanning laser ophthalmoscopy (AOSLO). They calculated the pore areas from the images and found that the total pore areas of LC in patients were larger than those in healthy subjects.

In addition, the volumetric data of LC has been studied in the past. Nadler et al. proposed a method for reconstructing a 3D image from a stack image using LC images from adaptive optics spectral domain-OCT (AO-SD-OCT) that have passed a segmentation process [6]. The characteristics of the LC structure were compared among three groups of samples: people with healthy eyes, glaucoma patients, and people at risk of glaucoma. The LC structure in the patients was found to have a smaller volume than that in the healthy eyes. The 3D image generated by AO-SD-OCT clearly showed the small structure and the contrast between the ROI and the background. However, there is a limitation that only a part of the LC can be seen in an image because of reflections of the tissue and blood vessels in front of the ONH.

Besides, we have reviewed how to improve the anatomical images of the eye, including the optic disc and cup, by computer techniques, i.e., image processing and machine learning techniques. Choukikar et al. applied simple image processing techniques, the thresholding technique, to separate the optic disc from enhanced images using histogram equalization. This approach is simple; however, it is inefficient when the image being analyzed has poor contrast or quality — the optic disc is not clearly visible [11]. However, the use of image processing techniques may not be sufficient for complex tasks. Therefore, there are many efforts to employ machine learning to tackle problems [7,8,12]. Almazroa et al. presented a method for segmentation of an optic disc image from a fundus image [12]. They applied level set and localization techniques to determine the extent of the optic disc and compare its accuracy. The edges were labeled by an ophthalmologist. The accuracy of the system was 83.9%. Mangipudi et al. presented a method for classifying optic disc and cup images using deep learning [8]. The U-shaped Encoder-Decoder Network (U-net) model was tested on three sets of data: DRISHTI-GS, DRIONS-DB, and RIM-ONE v3. The Intersection Over Unions (IoUs) were 96.6%, 96.2%, and 98.4% for the optic disc, respectively. However, there was still an issue with images where the optic disc or cup had low contrast with the background, and the model performed poorly on images with a small cup. Surendiran et al. also presented a method for classifying optic discs and cups [7]. They compared active contour segmentation with level set function, ANN, K-means, CNN, Fuzzy C-means, and a modified RNN that combined convolutional network with RNN on five data sets. The modified RNN was found to be the most efficient because they were able to capture the intra- and interslice contexts.

Moreover, the structure, porosity, and 3D visualization of LC have already been investigated. In studies by Akagi et al. [10] and Nadler et al. [6], it was found that using OCT with an application of adaptive optics produced clearer images. However, this achievement came with a high cost. Thus, the system was only used for research purposes, not usually used in an examination room.

This study aims to utilize images obtained from commercial OCT devices and employ computer techniques such as image processing and neural networks to enhance them and reconstruct 3D LC structures. The 3D LC structures can then be analyzed to differentiate between glaucomatous and non-glaucomatous eyes.

### 3. Materials and methods

The study was conducted at the Department of Ophthalmology, Faculty of Medicine, Chulalongkorn University, and King Chulalongkorn Memorial Hospital. The institutional review board of the Faculty of Medicine, Chulalongkorn University, in accordance with the Declaration

of Helsinki approved the research protocol, document number 149/61. The written informed consent was obtained from all participants.

### 3.1. Study population

In this study, the participating subjects were 58 healthy people and 65 glaucoma patients who underwent SS-OCT as part of their routine glaucoma follow-up at the Department of Ophthalmology, Faculty of Medicine, Chulalongkorn University and King Chulalongkorn Memorial Hospital. All healthy volunteers were selected under the following criteria: (1) no glaucomatous optic neuropathy or visual field defect; (2) no retinal, neuro-ophthalmological, psychological, or neurological disease that influences the ability to perform visual field analysis, fundus photography, and OCT; (3) spherical refractive error within  $\pm 6$  diopters and astigmatism less than three diopters; and (4) no history of eye trauma or intraocular surgery. Nevertheless, some cataract patients or patients after cataract surgery also participated in the study. The two groups of subjects who passed the criteria were over 18 years of age and had both eyes examined by the instruments listed in Table 1.

**Table 1. Methods of eye examination with the tools and criteria that were used to select samples**

Test	Medical Device		Reliability Criteria
	Algorithm	Device	
Visual field testing	SITA-standard 24-2	Humphrey Field Analyzer (Carl Zeiss Meditec, Dublin, CA)	- Fixation Loss < 20% - False Positive and Negative Error < 15%
	Optic disc cube 200x200	Cirrus HD-OCT 5000 (Carl Zeiss Meditec, Dublin, CA)	- Signal Strength Index > 6 - The edge of the Optic Disc must be clearly visible. - There are no black bars covering the image area.
OCT	3D wide	DRI OCT Triton (Topcon, Inc., Tokyo, Japan)	- There are no black bars covering the image area. - The cup is not too deep that holes will appear on the image.

### 3.2. OCT image acquisition

OCT is an instrument that uses the low coherence principle and detects reflected light signal after it was backscattered from the sample [13]. Generally, it is a Michelson Interferometry system. The light source is a broadband laser. There are two types of signal: (1) A-Scan is a signal that is detected at various depths of a sample, and (2) B-Scan is a signal generated from the unevenness of the refractive index at different depths in the sample. When the signal is rendered into an image, it will be a cross-section of the sample [14], shown in Fig. 1(a). The first generation of OCT was a time-domain OCT (TD-OCT) system that was slow. It has been developed into spectral-domain OCT (SD-OCT) and swept-source OCT (SS-OCT) by improving the transducer's sensitivity. At present, it is used in the medical and other industries. This research collected experimental image data from glaucoma patients and healthy individuals using two OCT devices: the DRI OCT Triton (SS-OCT type) and the Cirrus HD-OCT 500 (SD-OCT type).

**LC images** LC images of both eyes from DRI OCT Triton were captured with a 3D wide program and exported via the Enface algorithm in IMAGEnet6 software. The instrument had a light source with a wavelength of 1,050 nm and a scanning rate of 100,000 A-scans/sec. It had a resolution of 11.7  $\mu\text{m}/\text{pixel}$  in the axial scan. The image size was  $512 \times 384$  pixels. The exported images were a set of enface images, as shown in Fig. 1(b), and a cross-section image, as shown in Fig. 1(a). We selected only one eye image with a higher percentage of quality, as determined through the Enface algorithm. From all images, a specific set of Enface images, taken from the first image of the anterior LC surface down to the posterior LC surface as shown in Fig. 1(a), was then selected for further analysis. The anterior LC surface was located below the cup, where the

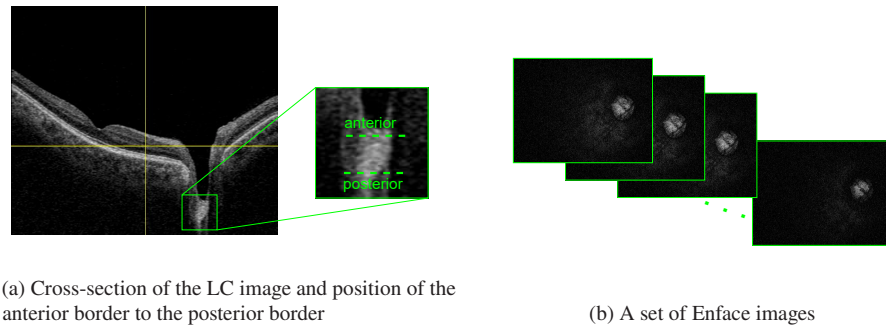


**Fig. 1.** Images of LC taken by the DRI-OCT, an SS-OCT type

tissue exhibited clear thickening in the highly reflective region until reaching the non-reflective region, which was the location of the posterior LC surface [15].

It should be noted that the functionality of images taken by SS-OCT was limited due to the presence of low-density LC tissues, which made it difficult to clearly define the extent of the LC, as shown in Fig. 1(b). As a result, the LC region in that area could not be accurately identified [16]. The LC is typically cylindrical within the optic disc and has the same boundary. Therefore, we utilized data from optic disc images obtained from HD-OCT, which had clear boundaries, to identify the extent of the LC in SS-OCT images.

**Optic disc images** Both eyes' optic disc images were enface images from Cirrus HD-OCT 5000 and a  $200 \times 200$  Optic disc cube program. OCT had a light source wavelength of 840 nm. The scanning rate was 27,000–68,000 A-scans/sec. The resulting image is  $562 \times 563$  pixels. Figures 2(a) and 2(b) show an example of an optic disc image taken by the HD-OCT and LC images taken by the DRI-OCT from the same eye, respectively.

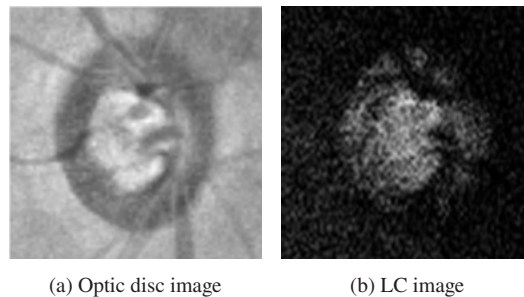


**Fig. 2.** Optic disc and LC images are taken from the same participant. The edges of the optic disc image are more clearly defined than that of the LC image.

When using the OCT tool to capture photos, it is important to ensure that the resulting images do not have black bars covering the image area caused by the participant moving their face away from the device while taking the image. Such black bars can lead to insufficient ROI information. Furthermore, it is important to consider the depth of the cup during image export. The exported images in this research only encompassed the region below the cup, as the focus was on the lower part. As previously mentioned, the anterior LC surface was immediately beneath the cup. However, due to the tool's limitations, exporting deep cup images down to the posterior LC surface was not feasible in some instances. The OCT used in the study had a scanning range of 12 mm, limiting the capture of samples with a distance between the cornea and the posterior LC



surface of less than 12 mm. Consequently, images of these samples were not eligible for further analysis.

### 3.3. Proposed experimental framework

In this section, we describe the methods used in the study process. They consisted of (1) optic disc segmentation in the optic disc image to be used as data for determining the edge of the LC from the LC image, (2) blood vessel removal from LC using the maximum principal curvature algorithm, (3) alignment of segmented optic disc image and LC image by image processing technique, and (4) 3D reconstruction, reconstructing LC images that have undergone all the above procedures to form a 3D structure. The proposed framework is illustrated in Fig. 3.

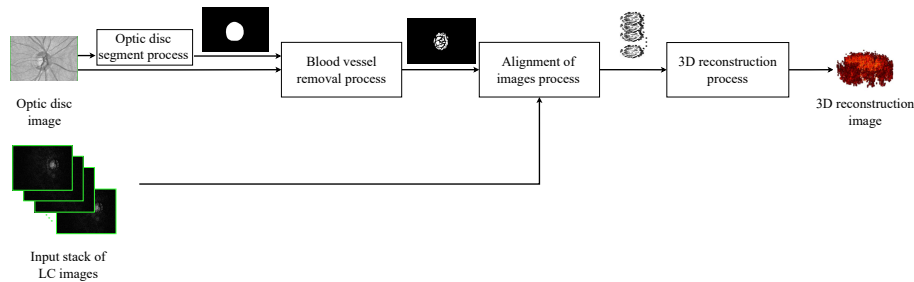


Fig. 3. Proposed Experimental Framework

**Optic Disc Segmentation** Initially, we evaluated the effectiveness of Gaussian filtering and image thresholding as a basic approach for segmenting LC images. However, the results revealed that certain edge information was absent in the regions where some LC tissues exhibited lower density than others. Consequently, the LC's boundary in those areas could not be accurately identified. Hence, to address the issue of missing edge information in LC images, we used an optic disc image to assist with edge detection. Specifically, we used a U-shaped Encoder-Decoder Network with Attention (Attn U-Net) model to segment the optic disc image and use the segmented optic disc image to identify the LC edge in the LC image accurately. Attn U-Net used the basic principles of U-Net but added an attention gate to weigh the feature maps from the skip connections, allowing the network to focus on more informative features and ignore less relevant ones [17]. The Attn U-Net architecture is illustrated in Fig. 4.

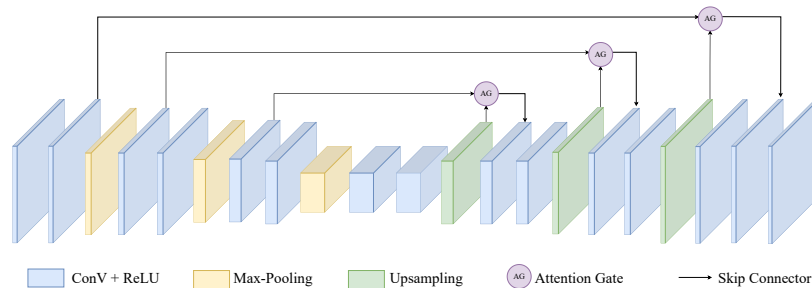
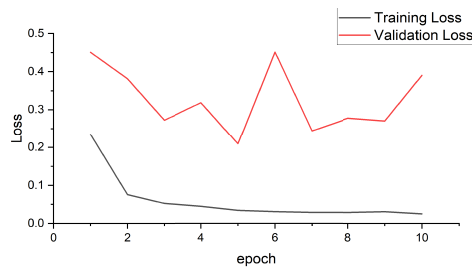


Fig. 4. Simplified schematic of Attn U-Net

In this step, we assigned the edges of the optic disc determined from the optic disc image to be the edges of the LC. Due to the small sample size, we employed a pre-trained Attn U-Net model [18] and fine-tuned it using our optic disc image dataset of 77 images, which were labeled with ground truth images using the LabelMe application [19] by a specialist ophthalmologist.

Although the labeled images could have been utilized for further analysis, we opted to employ segmented images generated by a segmentation model. This decision was motivated by our aim to develop an automated system capable of handling large sample sizes in the future. In this work, the dataset was divided into 80:10:10 for training, validation, and testing. While we understand the limitations of having a small number of test images, we have taken measures to address this concern. Instead of running the experiment only once with the limited test set, we conducted the experiment ten times with different random splits of the data. By doing so, we were able to generate a more comprehensive evaluation of our model's performance. The model was fine-tuned using the Adam optimizer with a learning rate of  $1 \times 10^{-6}$  with a small number of epochs. During the fine-tuning process, the model aimed to minimize the loss function, which utilized the cross-entropy loss. The optimal epoch was selected based on the lowest loss observed on the validation set. Subsequently, the optimal model was chosen based on the performance achieved at the optimal epoch.

In the overall picture, the model demonstrated impressive performance with an area under the receiver operating characteristic curve (AUROC) of  $0.97 \pm 0.03$  and a mean average precision (MAP) of  $0.90 \pm 0.07$ , across ten runs. These results highlight the promising performance of the model in accurately classifying and detecting the target variable. It is worth mentioning that our task is not excessively complex, and the utilization of a pre-trained model with fine-tuning on a relatively small number of annotated images contributes to achieving such performance. Additionally, the U-net model has shown promising performance even with a small number of annotated images, as reported in previous studies [20]. We randomly selected one model out of the ten available models and employed it for automatic segmentation. The model's cross-entropy loss function values on the training and validation sets are depicted in Fig. 5. It is evident that the model achieves its lowest loss after five epochs and starts to exhibit signs of overfitting thereafter. Therefore, the optimal model is selected at this epoch. The model performed well on the test set, achieving an AUROC of 0.97 and a MAP of 0.90. We also evaluated the model on the training and validation sets, with the following results: for the training set, ROC = 1.0 and MAP = 0.99, and for the validation set, ROC = 0.97 and MAP = 0.79. Overall, considering all sets (training, validation, and test), the model achieved a ROC of 0.99 and a MAP of 0.98. These metrics demonstrate a strong correlation between the predicted segmentations and the labeled images, providing confidence in the accuracy and reliability of our segmentation model for this study.



**Fig. 5.** Cross-Entropy loss on the training and validation sets of the model

**Blood Vessels Removal** To create an optic disc mask that removes the blood vessels, two potential options are color fundus images and enface optic disc images. However, in this work, we have chosen to utilize enface optic disc images for several reasons: (i) Enhanced Visualization: Enface optic disc images acquired through OCT scanning offer depth information and enable visualization of various components within the sample, such as the structure, optic cup, and blood vessels. This imaging modality provides a clearer representation of these components compared to color fundus images, which primarily emphasize the visualization of blood vessels.

(ii) **Boundary Accuracy:** The boundary of the optic disc obtained from color fundus images may not align precisely with the boundary derived from enface optic disc images. Color fundus images capture a wide-angle view, resulting in a smaller size (lower resolution) of the optic disc. Additionally, reflections from the lower part of the disc, known as the cup, can overlap with the disc boundary in color fundus images, making it challenging to differentiate between the two. Considering these factors, we have determined that utilizing enface optic disc images from OCT provides a more suitable and reliable approach for our work. This approach allows for accurate analysis of the optic disc region, including tasks such as segmentation and the removal of blood vessels.

The blood vessels were identified using the maximum principle of curvature algorithm [21]. However, when the maximum principle of curvature algorithm was directly applied to the image, small details were observed at the edges of the blood vessels, resulting in scattered white pixels throughout the images. To mitigate this issue, a Gaussian filter with a Gaussian width value of 3.5 was applied before utilizing the algorithm to eliminate these small details. Subsequently, the resulting optic disc mask, which removes the blood vessels, was aligned with the stack of LC images using our proposed alignment procedure. Figure 6 displays an example of the optic disc and its corresponding mask without the blood vessels.



**Fig. 6.** Blood vessel removal process; (a) optic disc image with optic disc segment image that applied Gaussian filter, and (b) optic disc segment image which removes the blood vessels

**Alignment** To map the optic disc segment image ( $I_{OD}$ ) — which is already removed the blood vessel — onto the LC image ( $I_{LC}$ ) obtained from different OCT machines, it was necessary to align them. The images obtained from the two machines differed in size and position of the LC due to the default settings of the tools, as well as in the angle of the LC due to the eyeball roll during shooting. Therefore, an alignment procedure was performed using image processing techniques. The procedure involved the following steps: (i) Automated ellipse detection on the  $I_{OD}$  image is performed using the *regionprops* function [22]. This function allows us to measure various properties of ellipse regions within the image. Specifically, we extract three key parameters: the length of the major axis ( $L_{OD}$ ), the angle between the major axis and the  $x$ -axis ( $\theta_{OD}$ ), and the center point of the ellipse ( $C_{OD}$ ). (ii) Given a series of  $N$  images of  $I_{LC,i}$  for each eye, where  $i = 1, \dots, N$ , the value of  $N$  is determined based on the distances between the anterior and posterior LC surfaces. These distances are obtained by an ophthalmologist using the software of the OCT tool. We calculate the average of the series  $I_{LC} = \frac{1}{N} \sum_{i=1}^N I_{LC,i}$ . Noted that each eye may have a different number of images. Because  $I_{LC}$  has a disordered distribution of white pixels, we applied a Gaussian filter with a Gaussian width  $\sigma$  of 3 to it and performed ellipse detection, obtaining three parameters:  $L_{LC}$ ,  $\theta_{LC}$ , and  $C_{LC}$ . (iii) Adjust the LC position on the  $I_{OD}$  and  $I_{LC}$  to be in the same  $(x, y)$  coordinates by adjusting  $C_{OD}$  to be in the same coordinates as the  $C_{LC}$ . (iv) Ensure that the major axis of the ellipse, as detected in image  $I_{OD}$ , aligns with that of image  $I_{LC}$ , this alignment is achieved by automatically rotating image  $I_{OD}$  so that the difference between the angles obtained from ellipse detection,  $\theta_{OD}$ , and  $\theta_{LC}$  (obtained from image  $I_{LC}$ ) is zero. (v) Adjust the size of the OD to the same size by adjusting the  $L_{OD}$  to be the same length as



$L_{LC}$ , obtaining a mask that identifies the extent of the LC in  $I_{LC,i}$ . (vi) Crop resulting  $I_{OD}$  and  $I_{LC}$  to cover the entire LC region by starting at  $C_{LC}$  and  $C_{OD}$  and cropping 45 pixels in each direction (left, right, top, and bottom). This results in  $\tilde{I}_{OD}$  and  $\tilde{I}_{LC,i}$  with a size of  $90 \times 90$ . (vii) Apply  $\tilde{I}_{OD}$  onto the  $\tilde{I}_{LC,i}$  leading to  $\tilde{I}_{LC,i} = \tilde{I}_{OD} \otimes \tilde{I}_{LC,i}$ . The above steps can be written in pseudocode as shown in Algorithm 1, and examples of each step are illustrated in Fig. 7.

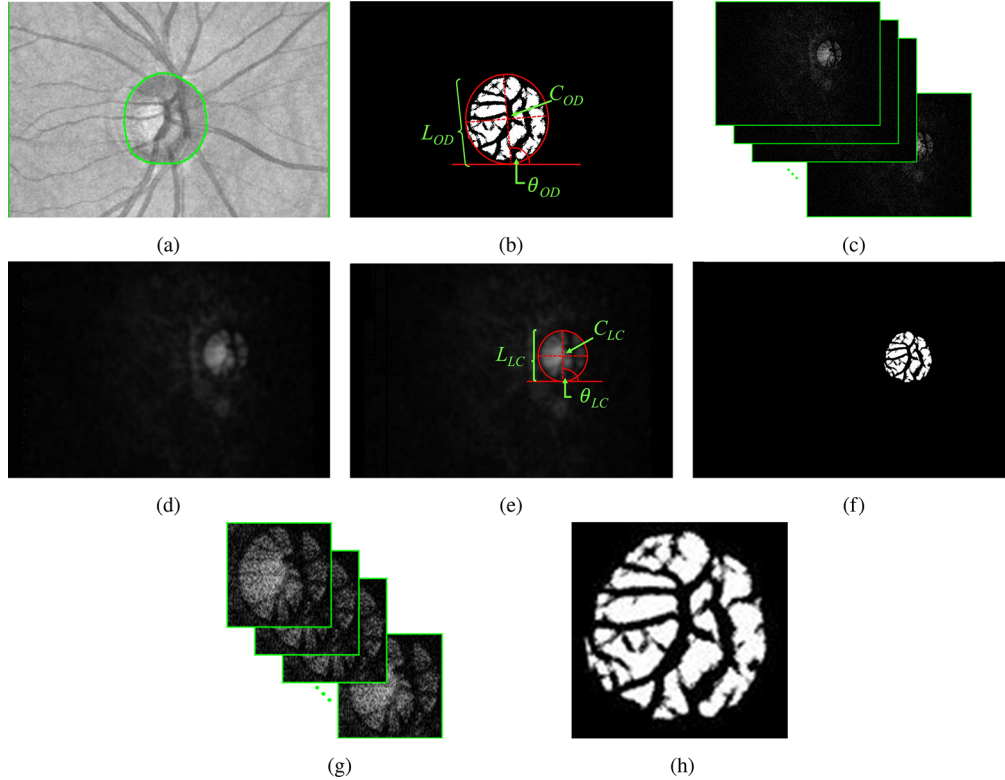


**Fig. 7.** Image alignment process: (a) input optic disc image with edge detection, (b) ellipse detection on the optic disc segment image, (c) input stack of LC images, (d) application of Gaussian filter on the LC image, (e) ellipse detection on the LC image, (f) shifting the optic disc segment image to the same coordinate as the LC image and rotating it until the major axis aligns with the LC image, (g) cropping the stack of LC images, and (h) cropping the optic disc segment image

**3D Reconstruction** In this process, a 3D LC image was generated from a stack of LC images using Matlab [23]. In the first step, a stack of LC images, represented as 2D arrays as shown in Fig. 8(a), was inputted and converted to a 3D array using the squeeze function. In the subsequent step, solid volumes were generated from the 3D array of LC images using the isosurface function, as shown in Fig. 8(b). Afterward, the resulting 3D LC reconstruction image was visualized using the volumeViewer function. For visualization, the display format was set to volume rendering, and the alphamap was selected as CT-soft tissue type, as shown in Fig. 8(c).

**Algorithm 1** Alignment Procedure

**Require:** Optic Disc Segment ( $I_{OD}$ ), a series of  $N$ -LC Image ( $I_{LC,i}$ ),  $i = 1, \dots, N$ , and Gaussian width ( $\sigma$ )

**Ensure:**  $N$ -Cropped LC Image ( $\hat{I}_{LC,i}$ ),  $i = 1, \dots, N$

- 1:  $[L_{OD}, C_{OD}, \theta_{OD}] = \text{Ellipse\_Detection}(I_{OD})$  ▷ Based on *regionprops* function
- 2:  $I_{LC} = \frac{1}{N} \sum_{i=1}^N I_{LC,i}$
- 3:  $I_G = \text{Gaussian}(I_{LC}, \sigma)$
- 4:  $[L_{LC}, C_{LC}, \theta_{LC}] = \text{Ellipse\_Detection}(I_G)$  ▷ Based on *regionprops* function
- 5: Shift  $C_{OD}$  to be in the same coordinate as  $C_{LC}$
- 6: Rotate  $I_{OD}$  until its major axis aligns with that of  $I_{LC}$
- 7: Calculate the scaling factor  $k = L_{OD}/L_{LC}$
- 8:  $I'_{OD} = \text{Resize}(I_{OD}, k)$
- 9:  $[\tilde{I}_{OD}, \tilde{I}_{LC,i}] = \text{Crop}(I'_{OD}, I_{LC,i})$
- 10:  $\hat{I}_{LC,i} = \tilde{I}_{OD} \otimes \tilde{I}_{LC,i}$
- 11: **return**  $\hat{I}_{LC,i}$

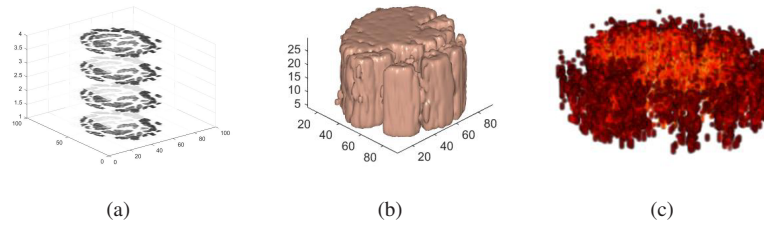


**Fig. 8.** 3D reconstruction process: (a) stack of LC images, (b) solid volume format, and (c) 3D reconstruction

## 4. Results and discussion

This section discusses two research findings: (1) the clinical study and (2) the three-dimensional LC structure of glaucomatous and non-glaucomatous eyes.

### 4.1. Clinical study

A comparison was conducted between the characteristics of LC in 65 glaucomatous eyes and 58 non-glaucomatous eyes (comprising 13 suspected glaucoma and 45 normal eyes). However, there were only 32 images of glaucoma eyes (49.2%) and 45 images of non-glaucoma eyes (77.6%) that met the criteria specified in Table 1. In diagnosing glaucoma, various characteristics within the study sample were considered. These include (i) Age, as glaucoma tends to be more prevalent in older individuals. It is important to note that it is ideal for the control group's age to be closely matched to the glaucomatous eyes group. However, finding non-glaucomatous volunteers with a similar age range proved to be challenging. The evidence indicated a change in the thickness of the human LC of about  $14 \mu\text{m}$  per 10 years [24]. Based on this information, we considered that the age difference between our two sample groups did not significantly impact the LC volume; (ii) Retinal nerve fiber layer thickness (RNFL), which progressively thins with advancing age [25]; (iii) Disc area; (iv) Cup-to-disc ratio, which was found to be higher in the glaucoma group compared to the non-glaucoma group [26]; (v) Cup volume, which exhibited greater volume in the glaucoma group [26]; and (vi) Visual field examination parameters, it was found that mean deviation and visual field index of the glaucoma group were lower [27]. Consequently, the parameters were collected, and the demographic data of the samples were summarized, as presented in Table 2.

**Table 2. Demographic Characteristics of the Study Sample — mean value  $\pm$  standard deviation**

Characteristic	Glaucoma ( $N = 32$ )	Non-glaucoma ( $N = 45$ )	$p$ -value
Age (year)	69.80 $\pm$ 10.40	61.20 $\pm$ 11.50	0.002 <sup>a</sup>
OCT parameters			
Average RNFL ( $\mu\text{m}$ )	73.90 $\pm$ 14.90	92.70 $\pm$ 10.20	< 0.001 <sup>b</sup>
Disc area ( $\text{mm}^2$ )	2.00 $\pm$ 0.49	2.09 $\pm$ 0.43	0.533 <sup>b</sup>
Cup-to-disc ratio	0.73 $\pm$ 0.09	0.60 $\pm$ 0.12	< 0.001 <sup>a</sup>
Cup volume ( $\text{mm}^3$ )	0.45 $\pm$ 0.29	0.26 $\pm$ 0.21	0.001 <sup>b</sup>
Visual field parameters			
Mean deviation (dB)	-7.69 $\pm$ 7.37	-1.25 $\pm$ 2.49	0.001 <sup>b</sup>
Pattern standard deviation (dB)	6.39 $\pm$ 4.64	1.94 $\pm$ 0.59	< 0.001 <sup>b</sup>
Visual field index (%)	78.70 $\pm$ 24.32	97.77 $\pm$ 3.14	< 0.001 <sup>b</sup>

<sup>a</sup>independent  $t$ -test<sup>b</sup>Mann-Whitney U test

According to Table 2, significant differences were found in most of the characteristics between the two groups ( $p < 0.05$ ) using an independent  $t$ -test for normally distributed data and Mann-Whitney U test for non-parametric data, except disc area did not show a significant difference in the sample groups ( $p = 0.533$ ). This may be due to the variation in disc area size among individuals. Instead, the unit norm of disc area, calculated through the cup-to-disc ratio [26], should be considered.

In typical glaucoma studies, the LC structure is divided into four quadrants: Superior ( $Q_S$ ), Inferior ( $Q_I$ ), Nasal ( $Q_N$ ), and Temporal ( $Q_T$ ). Significant differences were observed in the pore area within the Superior ( $Q_S$ ) and Inferior ( $Q_I$ ) quadrants between glaucoma and non-glaucoma eyes [10]. Additionally, tissue loss was observed in the  $Q_S$  and  $Q_I$  quadrants during the early stages of glaucoma [28]. To investigate the significant differences between glaucoma and non-glaucoma eyes in more detail, we further divided the areas of  $Q_S$ ,  $Q_I$ ,  $Q_N$ , and  $Q_T$  quadrants. The LC structure was divided into 12-clock-hour sectors, as illustrated in Fig. 9. Specifically, the  $Q_S$  quadrant encompassed sectors  $S_1$ ,  $S_{11}$ , and  $S_{12}$ , while the  $Q_I$  quadrant included sectors  $S_5$ ,  $S_6$ , and  $S_7$ .

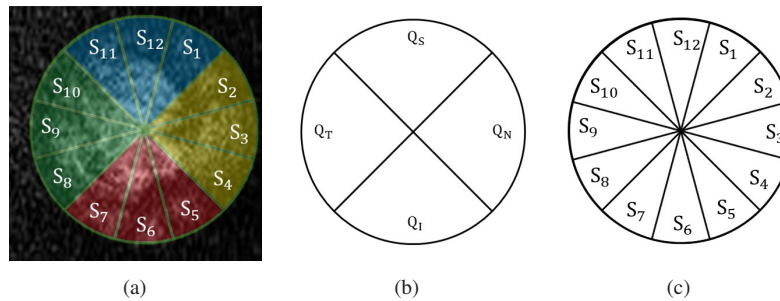


**Fig. 9.** (a) LC with divided areas; the blue, yellow, red, and green regions represent the  $Q_S$ ,  $Q_N$ ,  $Q_I$ , and  $Q_T$ , respectively, (b) Illustration of the quadrants, and (c) Illustration of the 12-clock-hour sectors of the right eye

This study investigated the differences in the LC between glaucoma and non-glaucoma eyes by analyzing specific LC characteristics, namely LC volume, pore volume, and pore-to-LC volume. LC volume can be calculated as  $\sum_{i=1}^N W(\hat{l}_{LC,i})$ , pore volume that refers to the volume occupied

by the pores or void spaces within the LC structure, can be calculated as  $\sum_{i=1}^N B(\hat{I}_{LC,i})$ , when  $N$  represents the number of LC images, and  $W(\cdot)$  and  $B(\cdot)$  represent the counts of white and black pixels in an image, respectively. A white pixel is defined when the intensity of the pixel in an LC image is greater than or equal to a threshold  $T$ , while a black pixel is defined as having an intensity less than the threshold  $T$ .  $T$  is manually defined by an ophthalmologist who carefully selects 12 LC images from different subjects, each with clearly visible pores, as depicted in Fig. 10(a). The ophthalmologist adjusts  $T$  to 55, ensuring that the considering pores are distinctly visible. To visually demonstrate the effect of the thresholding process, Fig. 10(b) showcases the binarized LC images corresponding to the original images shown in Fig. 10(a). The pore-to-LC volume is calculated as a percentage of the pore volume relative to the LC volume. These three characteristics were extracted from the 3D representation of the LC obtained through the procedure described in Section 3.3. These metrics are expressed in voxel units. The calculation of these characteristics was performed for each section within the structural division considered, which encompassed the overall LC (referred to as “overall”), the individual quadrants (referred to as “quadrants”), and the proposed sector-based division (referred to as “sectors”).

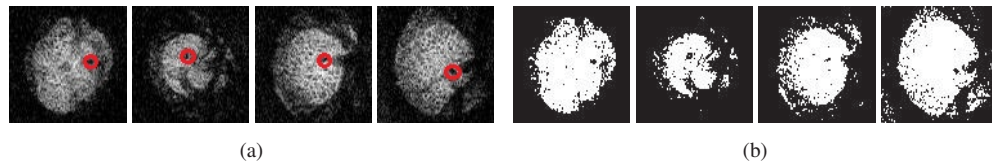


**Fig. 10.** (a) The pore area identified by an ophthalmologist and (b) binarized LC images obtained by applying the threshold  $T$

According to Table 3, an analysis of the overall structure revealed that the glaucoma group exhibited a mean of 57,840.6 voxels, whereas the non-glaucoma group demonstrated a mean of 70,967 voxels. This comparison yielded a statistically significant difference ( $p < 0.05$ ) as determined by an independent  $t$ -test, considering the normal distribution of the data. Similarly to the pore volume, the glaucoma group had a mean of 2,160.9 voxels, whereas the non-glaucoma group had a mean of 4,243.7 voxels, demonstrating a significant difference, determined using the Mann-Whitney U test due to the non-normal distribution of the data. However, the main difference in LC and pore volume is primarily influenced by the height of the LC volume. In our data collection process, we observed distinct differences in the LC heights between the two groups of samples. To account for the effect of height and provide a more comprehensive analysis, we also consider the volumetric data of the LC and pores. In particular, we calculate the pore-to-LC volume, which allows us to consider the pore volume in relation to one unit of LC volume. This value provides insights into the relationship between pore volume and the overall LC volume, helping to assess the significance of the pore structure within the context of LC characteristics. The glaucoma group exhibited a mean of 3.6, while the non-glaucoma group showed a mean of 5.8. This difference was also statistically significant, analyzed using the Mann-Whitney U test. Overall, the findings highlight significant disparities in the total LC structure, pore volume, and pore-to-LC volume characteristics between glaucoma and non-glaucoma groups, reinforcing the potential value of these parameters in distinguishing between the two conditions.

Considering the division of glaucomatous and non-glaucomatous eyes into quadrants, the independent  $t$ -test revealed significant differences in the LC volume. At the same time, the Mann-Whitney U test indicated significant differences in both the pore volume and pore-to-LC volume in most of the quadrants ( $p < 0.05$ ). However, it is worth noting that in quadrant  $Q_T$ , the difference in the LC volume between glaucoma and non-glaucoma cases reached a significance level of  $p = 0.054$ . This finding is consistent with a previous study [29], which reported the slowest decline of tissues in this specific quadrant. Additionally, significant differences were

**Table 3. Comparison of the LC characteristics in glaucomatous and non-glaucomatous eyes, analyzed in terms of overall, quadrant, and sector divisions. The reported values represent the mean values along with their corresponding standard deviations. It is important to highlight that the pore-to-LC volume was individually calculated for each sample and subsequently averaged.**

Division	LC volume (voxel) <sup>a</sup>			Pore volume (voxel) <sup>b</sup>			Pore to LC volume (%) <sup>b</sup>		
	Glaucoma	Non-glaucoma	<i>p</i> -value	Glaucoma	Non-glaucoma	<i>p</i> -value	Glaucoma	Non-glaucoma	<i>p</i> -value
Overall	57,840.6±2995.6	71,967.0±2721.3	< 0.001	2,160.9±226.8	4,243.7±273.0	< 0.001	3.6±0.3	5.8±0.3	< 0.001
Quadrants									
Q <sub>S</sub>	14,643.3±773.9	19,396.6±733.2	< 0.001	622.0±64.2	1,269.8±97.9	0.004	4.1±0.3	6.4±0.4	< 0.001
Q <sub>I</sub>	14,859.1±779.4	19,358.2±730.6	< 0.001	517.3±72.8	1,175.6±95.7	< 0.001	3.3±0.3	5.9±0.4	< 0.001
Q <sub>N</sub>	13,392.6±703.4	16,251.8±711.6	< 0.001	713.0±93.4	1,248.6±93.3	< 0.001	5.1±0.5	7.6±0.4	< 0.001
Q <sub>T</sub>	14,945.7±803.0	17,060.3±707.0	0.054	308.5±26.3	549.8±43.9	0.021	2.1±0.2	3.4±0.3	< 0.001
Sectors									
S <sub>1</sub>	4,083.4±236.8	5,088.8±213.7	0.003	205.4±25.9	386.5±32.7	< 0.001	4.7±0.4	7.5±0.5	< 0.001
S <sub>2</sub>	4,066.2±226.8	4,949.0±223.7	0.009	215.2±32.5	357.4±29.9	< 0.001	5.0±0.6	7.1±0.4	< 0.001
S <sub>3</sub>	4,928.3±290.5	6,245.6±304.6	0.011 <sup>b</sup>	267.8±37.2	478.9±39.2	< 0.001	5.2±0.5	7.8±0.4	< 0.001
S <sub>4</sub>	4,398.1±218.4	5,057.2±249.5	0.231 <sup>b</sup>	230.0±26.4	412.2±35.0	< 0.001	5.1±0.4	8.1±0.5	< 0.001
S <sub>5</sub>	4,084.9±213.3	5,290.8±212.5	< 0.001	208.6±28.2	451.4±35.3	< 0.001	4.9±0.5	8.3±0.5	< 0.001
S <sub>6</sub>	6,165.3±307.8	8,092.8±338.2	< 0.001	190.1±30.0	490.3±50.6	< 0.001	2.9±0.3	5.8±0.5	< 0.001
S <sub>7</sub>	4,608.8±286.5	5,974.6±252.4	< 0.001	118.6±20.9	233.9±24.3	< 0.001	2.4±0.3	3.9±0.3	< 0.001
S <sub>8</sub>	4,696.5±578.5	5,586.4±252.4	0.034 <sup>b</sup>	96.2±12.7	199.1±17.5	< 0.001	2.0±0.2	3.7±0.3	< 0.001
S <sub>9</sub>	6,197.8±313.7	6,800.2±283.3	0.163	112.7±11.6	194.1±19.9	0.008	2.0±0.2	3.0±0.3	0.139
S <sub>10</sub>	4,051.4±244.1	4,673.8±221.4	0.067	99.6±10.7	156.6±13.2	0.002	2.4±0.2	3.5±0.3	< 0.001
S <sub>11</sub>	4,640.7±254.1	6,396.4±254.3	< 0.001	138.1±13.9	324.7±25.7	< 0.001	2.9±0.2	5.0±0.3	< 0.001
S <sub>12</sub>	5,919.2±306.3	7,911.4±305.8	< 0.001	278.5±30.5	558.6±54.1	< 0.001	4.5±0.4	6.8±0.5	< 0.001

<sup>a</sup>independent *t*-test

<sup>a</sup>Mann-Whitney U test

observed in the LC volume within quadrant Q<sub>N</sub>, characterized by a high density of blood vessels. By applying our method, which involved the removal of blood vessels, we could calculate the LC structure and porosity within this region, facilitating tissue visualization in Q<sub>N</sub>. Notably, the tissues in quadrant Q<sub>I</sub> and Q<sub>N</sub> are closely situated, suggesting that the deterioration of tissues in Q<sub>I</sub> may have a corresponding impact on the tissues in Q<sub>N</sub>. Again, these observations underscore the significance of quadrant-specific analysis, revealing distinct characteristics of the LC structure and highlighting the impact of tissue degeneration in different quadrants.

Next, the sector division structure was employed to analyze the differences between glaucoma and non-glaucoma groups. An independent *t*-test was conducted to compare the LC volume of each sector, except for sectors S<sub>3</sub>, S<sub>4</sub>, and S<sub>8</sub>, where the Mann-Whitney U test was utilized. Significant differences were observed between the two groups in all sectors, except for sectors S<sub>4</sub>, S<sub>9</sub>, and S<sub>10</sub>. Sectors S<sub>9</sub> and S<sub>10</sub>, situated in quadrant Q<sub>T</sub>, exhibited no differences between the groups, which aligns with the analysis conducted at the quadrant level. Interestingly, sector S<sub>4</sub>, located in quadrant Q<sub>N</sub>, showed no difference. This outcome can be attributed to the significant removal of blood vessels in this quadrant, resulting in similar and relatively small average LC volumes in both sample groups. Next, the Mann-Whitney U test was employed to analyze the pore volume characteristics in all sectors, revealing significant differences across the board. The calculations indicated that glaucomatous eyes had a lower pore volume than non-glaucomatous eyes. Among the glaucoma group, sector S<sub>12</sub>, located in Q<sub>S</sub>, showed the largest pore volume.

According to Table 3, we observed significant differences in LC volume between the two groups in all sectors, except for sectors S<sub>4</sub>, S<sub>9</sub>, and S<sub>10</sub>. In terms of pore volume, there was a significant difference between the two sample groups in all sectors. When comparing the



pore-to-LC volume as a normalized measure, we found a significant difference between the two sample groups in all sectors, except for  $S_9$ . Therefore, sector  $S_9$  is the only sector that did not exhibit any differences between the two sample groups.

Moreover, the results demonstrate that the LC volume and pore volume of the glaucoma group were significantly lower than those of the non-glaucoma group by approximately 20-25% ( $p < 0.001$ ) and approximately 50% ( $p < 0.001$ ), respectively. Typically, there is a correlation between LC area and pore area [30]. Therefore, it can be expected that the differences in LC volume and pore volume between glaucoma and non-glaucoma groups from the same set would be comparable. In this study, we observed a clear reduction in pore volume in the glaucoma group compared to the non-glaucoma group. This could be attributed to excluding blood vessels from the 3D LC in the vertical direction, potentially neglecting the underlying pores beneath the blood vessels. Consequently, the pore volume was lower than expected, resulting in a lower pore-to-volume in the glaucoma group compared to the non-glaucoma group.

Additionally, the study investigated the relationship between disc area and LC volume. It was observed that individuals with a smaller disc area tended to have a smaller LC volume, while those with a larger disc area exhibited a larger LC volume, as reported in a previous study by Hoffmann et al. [31]. To explore this relationship, linear regression analysis was conducted. The results indicated a significant correlation between disc area and LC volume in all areas examined, suggesting that disc area influences the size of the LC ( $p < 0.05$ ). Importantly, there were no significant differences in disc area between glaucoma and non-glaucoma groups.

#### 4.2. 3D visualization

The 3D structure images of the LC in glaucomatous and non-glaucomatous eyes were generated from OCT images using the method described in Section 3.3, as illustrated in Fig. 11. Our findings revealed that:

- (1) The thickness of the LC structure exhibited clear differences between the two sample groups. Specifically, the LC thickness in the non-glaucoma group was greater than that in the glaucoma group, which aligns with the data collected from the samples — the average LC thickness was 188  $\mu\text{m}$  for glaucomatous eyes and 289  $\mu\text{m}$  for non-glaucomatous eyes.
- (2) The density of the LC structure exhibited clear differences between the two sample groups. In this context, the density refers to the distribution of LC tissue (voxels) within the LC cylindrical structure. The structure of the non-glaucoma group was denser than that of the glaucoma group, which could be visually observed. By considering the division of the LC into quadrants and sectors, we found the following:
  - (i) Regions  $S_4$  and  $S_5$ , situated in the  $Q_N$  and  $Q_I$  quadrants of the LC, respectively, exhibited tissue degeneration. This observation was supported by the lower density of structures in these regions compared to the non-glaucoma group, aligning with the findings of the clinical study.
  - (ii) Tissue degeneration was found in the  $Q_S$  area, but it was not noticeable. However, a significant difference was found when calculating the volume and comparing the difference using the independent  $t$ -test method as shown in Table 3.
  - (iii) The edge of the LC tissue in glaucomatous eyes was challenging to define due to the larger cup size in the glaucoma group. This led to the displacement of blood vessels towards the edge of the LC, making it challenging to determine the boundaries accurately.

In our study, several limitations were encountered. Firstly, we did not utilize the  $3\text{mm} \times 3\text{mm}$  or  $6\text{mm} \times 6\text{mm}$  scan modes, which are available on our machine, due to computational

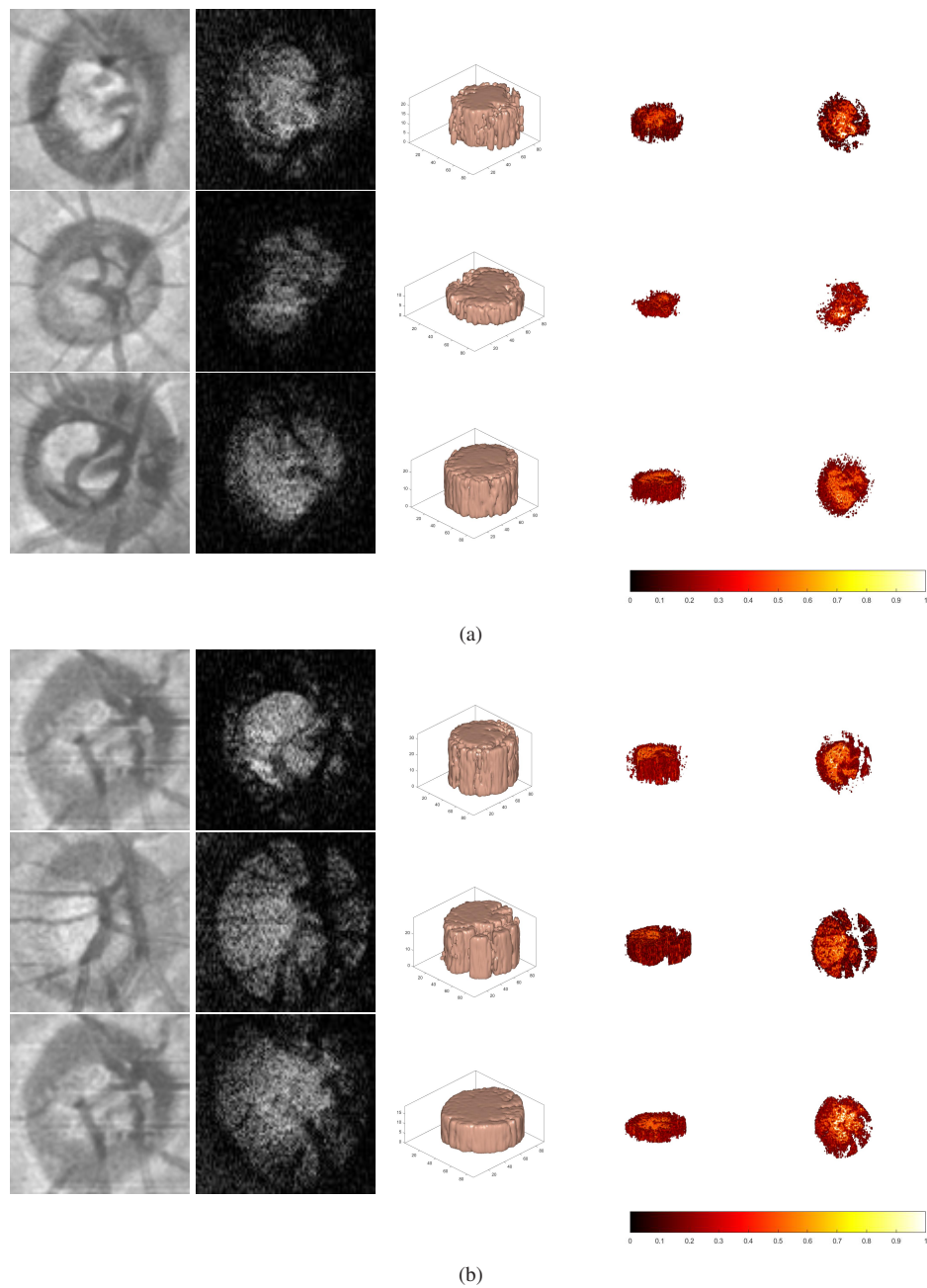


**Fig. 11.** Optic disc image, LC image, 3D LC reconstruction in solid volume, side view of 3D LC rendering image, and top view of 3D LC rendering image of (a) glaucomatous eyes and (b) non-glaucomatous eyes. The color bar indicates the density, with dark colors representing low density and bright colors representing high density.

constraints and limitations of our computing resources. Instead, we opted for the wider scan mode of  $12\text{mm} \times 9\text{mm}$  to reduce information density and alleviate the computational burden. While this decision facilitated the completion of 3D image reconstruction within our computer system's capabilities, it may have resulted in lower-resolution images. Although the narrower scan mode could potentially offer higher resolution and more accurate results, we made a practical adjustment considering the constraints we faced in data collection and processing. Another limitation we faced was the difficulty in automatically identifying the anterior and posterior lamina surfaces in the LC images obtained using SS-OCT. Manual intervention or additional processing steps were required to identify these surfaces, which added complexity to our analysis. Additionally, our study encountered a limitation in evaluating the performance of the blood vessel removal technique. Due to the absence of labeled images to assess performance, we were unable to conduct a comprehensive evaluation. This limitation highlights the need for future research. Due to the limited data sample size, relying solely on quantitative analysis conducted on the test samples would compromise the statistical power and robustness of our analysis. Consequently, we expanded our analysis to include all available samples, including those used in the segmentation model. However, it is worth noting that we have provided the performance of the model on the training and validation sets as well. These results demonstrate a strong correlation between the predicted segmentations and the labeled images, indicating accuracy and reliability in our findings. Lastly, we analyzed the LC pore and volume from the layer with complete optic nerve tissue. Therefore, images with deep cupping, usually found in advanced glaucoma, were excluded.

## 5. Conclusion

This research focused on reconstructing 3D LC images obtained from SS-OCT scans of glaucomatous and non-glaucomatous eyes. The study examined three key characteristics: LC volume, pore volume, and pore-to-volume. These characteristics were calculated based on dividing the LC structure into three levels: overall, quadrants, and sectors. The 3D LC reconstruction images revealed noticeable differences between the two sample groups, which aligned with significant differences observed in all three characteristics. Specifically, the degeneration of the LC structure was observed in quadrants  $Q_S$ ,  $Q_I$ , and  $Q_N$ , which coincided with the significant differences in LC volumes in these quadrants. Furthermore, significant differences were found in specific sectors:  $S_1$ ,  $S_{11}$ , and  $S_{12}$  in  $Q_S$ ;  $S_2$  and  $S_3$  in  $Q_N$ ; and  $S_5$ ,  $S_6$ , and  $S_7$  in  $Q_I$ . Analysis of pore volume characteristics also revealed significant differences between the two groups, with similar trends observed for the pore-to-LC volume, except for sector  $S_9$ . In summary, this study demonstrated distinct differences in glaucomatous and non-glaucomatous eyes regarding LC volume, pore volume, and pore-to-LC volume across various regions of interest.

**Funding.** School of Science, King Mongkut's Institute of Technology Ladkrabang (RA/TA-2562-M-029); School of Information Technology, King Mongkut's Institute of Technology Ladkrabang; Faculty of Medicine, Chulalongkorn University (Ratchadapiseksompotch Fund).

**Disclosures.** The authors declare no conflicts of interest.

**Data availability.** Data underlying the results presented in this paper are not publicly available at this time but may be obtained from the authors upon reasonable request.

## References

1. S. Yousefi, L. R. Pasquale, M. V. Boland, and C. A. Johnson, "Machine-identified patterns of visual field loss and an association with rapid progression in the ocular hypertension treatment study," *Ophthalmology* **129**(12), 1402–1411 (2022).
2. S. M. Prea, A. J. Vingrys, and G. Y. X. Kong, "Test reliability and compliance to a twelve-month visual field telemedicine study in glaucoma patients," *J. Clin. Med.* **11**(15), 4317 (2022).
3. O. Komolafe, O. Omolase, C. Bekibele, O. Ogunleye, O. Komolafe, and F. Omotayo, "Awareness and knowledge of glaucoma among workers in a Nigerian tertiary health care institution," *Middle East Af. J. Ophthalmol.* **20**(2), 163–167 (2013).

4. R. N. Weinreb, T. Aung, and F. A. Medeiros, "The pathophysiology and treatment of glaucoma: a review," *JAMA* **311**(18), 1901–1911 (2014).
5. M. Pircher and R. J. Zawadzki, "Review of adaptive optics oct (AO-OCT): principles and applications for retinal imaging," *Biomed. Opt. Express* **8**(5), 2536–2562 (2017).
6. Z. Nadler, B. Wang, G. Wollstein, J. E. Nevins, H. Ishikawa, R. Bilonick, L. Kagemann, I. A. Sigal, R. D. Ferguson, A. Patel, D. X. Hammer, and J. S. Schuman, "Repeatability of in vivo 3D lamina cribrosa microarchitecture using adaptive optics spectral domain optical coherence tomography," *Biomed. Opt. Express* **5**(4), 1114–1123 (2014).
7. J. Surendiran, S. Theetchenya, P. M. B. Mansingh, M. D. G. Sekar, N. Yuvaraj, V. J. Arulkarthick, C. Suresh, A. Sriram, K. Srihari, and A. Alene, "Segmentation of optic disc and cup using modified recurrent neural network," *BioMed Res. Int.* **2022**, 1–8 (2022).
8. P. S. Mangipudi, H. M. Pandey, and A. Choudhary, "Improved optic disc and cup segmentation in glaucomatous images using deep learning architecture," *Multimed. Tools Appl.* **80**(20), 30143–30163 (2021).
9. G. Tezel, K. Trinkaus, and M. B. Wax, "Alterations in the morphology of lamina cribrosa pores in glaucomatous eyes," *Br. J. Ophthalmol.* **88**(2), 251–256 (2004).
10. T. Akagi, M. Hangai, K. Takayama, A. Nonaka, S. Ooto, and N. Yoshimura, "In vivo imaging of lamina cribrosa pores by adaptive optics scanning laser ophthalmoscopy," *Invest. Ophthalmol. Visual Sci.* **53**(7), 4111–4119 (2012).
11. P. Choukikar, A. K. Patel, and R. S. Mishra, "Segmenting the optic disc in retinal images using thresholding," *Int. J. Comput. Appl.* **94**(11), 6–10 (2014).
12. A. Almazroa, W. Sun, S. Alodhayb, K. Raahemifar, and V. Lakshminarayanan, "Optic disc segmentation for glaucoma screening system using fundus images," *Clin. Ophthalmol.* **11**, 2017–2029 (2017).
13. D. Huang, E. A. Swanson, C. P. Lin, J. S. Schuman, W. G. Stinson, W. Chang, M. R. Hee, T. Flotte, K. Gregory, C. A. Puliaito, and J. G. Fujimoto, "Optical coherence tomography," *Science* **254**(5035), 1178–1181 (1991).
14. C.-L. Chen and R. K. Wang, "Optical coherence tomography based angiography [invited]," *Biomed. Opt. Express* **8**(2), 1056–1082 (2017).
15. A. Paulo, P. G. Vaz, D. A. D. Jesus, L. S. Brea, J. V. Eijgen, J. Cardoso, T. van Walsum, S. Klein, I. Stalmans, and J. B. Breda, "Optical coherence tomography imaging of the lamina cribrosa: Structural biomarkers in nonglaucomatous diseases," *J. Ophthalmol.* **2021**, 1–31 (2021).
16. K. Omodaka, T. Horii, S. Takahashi, T. Kikawa, A. Matsumoto, Y. Shiga, K. Maruyama, T. Yuasa, M. Akiba, and T. Nakazawa, "3d evaluation of the lamina cribrosa with swept-source optical coherence tomography in normal tension glaucoma," *PLoS One* **10**(4), e0122347 (2015).
17. O. Oktay, J. Schlemper, L. L. Folgoc, M. C. H. Lee, M. P. Heinrich, K. Misawa, K. Mori, S. G. McDonagh, N. Y. Hammerla, B. Kainz, B. Glocker, and D. Rueckert, "Attention U-Net: Learning where to look for the pancreas," *arXiv*, arXiv:1804.03999 (2018).
18. K. Xing and D. Hereñú, "Optic-disc-unet," Github, 2019, <https://github.com/DeepTrial/Optic-Disc-Unet>.
19. B. Russell, A. Torralba, K. Murphy, and W. Freeman, "LabelMe: A database and web-based tool for image annotation," *Int. J. Comput. Vis.* **77**(1-3), 157–173 (2008).
20. O. Ronneberger, P. Fischer, and T. Brox, "U-Net: Convolutional networks for biomedical image segmentation," in *Medical Image Computing and Computer-Assisted Intervention*, vol. 9351 of *LNCS* (Springer, 2015), pp. 234–241.
21. A. Iroshan, "Segmentation of blood vessels in retinal fundus images using maximum principal curvature," Mathworks, 2017, <https://www.mathworks.com/matlabcentral/fileexchange/64884-segmentation-of-blood-vessels-in-retinal-fundus-images-using-maximum-principal-curvature>.
22. MathWorks, Inca., "regionprops," MathWorks, 2023, <https://www.mathworks.com/help/images/ref/regionprops.html>.
23. MATLAB, 9.10.0.2198249 (R2021a) (The MathWorks Inc., 2021).
24. A. Kotecha, S. Izadi, and G. Jeffery, "Age-related changes in the thickness of the human lamina cribrosa," *The Br. J. Ophthalmol.* **90**(12), 1531–1534 (2006).
25. A. A. Jammal, S. I. Berchuck, A. C. Thompson, V. P. Costa, and F. A. Medeiros, "The effect of age on increasing susceptibility to retinal nerve fiber layer loss in glaucoma," *Invest. Ophthalmol. Visual Sci.* **61**(13), 8 (2020).
26. J. C. Tsai, "How to evaluate the suspicious optic disc," *Rev. Ophthalmol.* (2005).
27. I. Forchheimer, C. C. de Moraes, C. G. and Teng, F. Folgar, C. Tello, R. Ritch, and J. M. Liebmann, "Baseline mean deviation and rates of visual field change in treated glaucoma patients," *Eye* **25**(5), 626–632 (2011).
28. R. Sihota, G. Srinivasan, T. Dada, V. Gupta, D. Ghate, and A. Sharma, "Is the ISNT rule violated in early primary open-angle glaucoma—a scanning laser tomography study," *Eye* **22**(6), 819–824 (2008).
29. N. Harizman, C. Oliveira, A. Chiang, C. Tello, M. Marmor, R. Ritch, and J. M. Liebmann, "The ISNT rule and differentiation of normal from glaucomatous eyes," *Arch. Ophthalmol.* **124**(11), 1579–1583 (2006).
30. J. B. Jonas, C. Y. Mardin, U. Schlötzer-Schrehardt, and G. O. Naumann, "Morphometry of the human lamina cribrosa surface," *Invest. Ophthalmol. Visual Sci.* **32**(2), 401–405 (1991).
31. E. M. Hoffmann, L. M. Zangwill, J. G. Crowston, and R. N. Weinreb, "Optic disk size and glaucoma," *Surv. Ophthalmol.* **52**(1), 32–49 (2007).